Magnetic domains and unusual hysteresis loops of yttrium iron garnet crystals revealed by magneto-optic effects

View Online   Export Citation   CrossMark

X. D. Zhu[a] (iD)

AFFILIATIONS

Department of Physics and Astronomy, University of California, Davis, California 95616, USA and Department of Optical Sciences and Engineering, Fudan University, Shanghai 200045, China

[a]Author to whom correspondence should be addressed: xdzhu@physics.ucdavis.edu

ABSTRACT

I present a magneto-optic effect study of magnetic domains in a ferrimagnetic yttrium iron garnet crystal at different stages of a hysteresis loop. By measuring the Faraday effect in response to the out-of-plane component and Kerr effects to the in-plane components of the sample magnetization, I examined the evolution of magnetic domains during a hysteresis loop in an in-plane external magnetic field. I found that crystalline anisotropy, magneto-static energy, and the presence of movable domain walls play indispensable roles in the domain orientation, particularly when the external field is near zero, and have led to seemingly unusual appearances of hysteresis loops.

I. INTRODUCTION

Ferromagnetic and ferrimagnetic states are important phases of solids. They are present in many materials of practical utility and in new quantum materials, often at low temperatures or under high pressures. Combined with first-principles theories, the experimental investigations of ferromagnetic states of crystalline solids are crucial steps toward understanding mechanisms that drive the emergence of ferromagnetism. Theoretical models are usually based on homogeneous solids with perfect crystallinity. In practice, as-grown samples are spatially inhomogeneous. As a result, the onsets and characteristics of magnetic properties are expected to vary from one part to another part of a sample. Domains with different magnetic orientations and separated by movable domain walls can be formed even within a homogeneous region of a sample. This is driven by the propensity to the lowest total free energy configuration, especially when the external field is weak or absent. Crystalline anisotropy, shape anisotropy, domain wall energy, magneto-static energy, and inhomogeneity in a sample are some of the major factors that determine the orientation and distribution of magnetic domains. Experimentally, measurements of magnetization and magnetic susceptibility are typically done on a whole sample and thus yield averaged magnetic properties. Such an average varies when the inhomogeneity and resultant magnetic domain structures change from one sample to another, making separation of intrinsic ferromagnetic properties from those arising from inhomogeneity a difficult task at times. As a result, spatially resolved magnetic measurements are needed and should be performed, when feasible. This facilitates efforts to understand mechanisms that lead to ferromagnetic states and intrinsic characteristics and to connect these intrinsic properties with the averaged behaviors of a sample as a whole.

The optical characterization of a sample magnetization through magneto-optic (MO) effects meets such experimental needs.[1–6] The microscopic measurements of MO effects can resolve the sample magnetization with a spatial resolution limited only by the optical wavelength. In addition, unlike magnetic force microscopy (MFM)[7–10] and x-ray magnetic dichroism (XMCD) microscopy[11–15] that do not determine the full vector characteristics of a sample magnetization, magneto-optic effects arising from different components of the magnetization are distinguishable. As a result, suitably designed magneto-optic measurements enable a full characterization of a sample magnetization vector, even in the absence of an external polarizing magnetic field.

In this work, I report a magneto-optic effect study of an yttrium iron garnet (YIG) single crystal sample, YIG(100) disc, during hysteresis loops. The external magnetic field is applied in the plane of the sample surface. The sample magnetization is measured through magneto-optic effects using two Sagnac-interferometry based optical detection systems.[5,6] One measures the Faraday effect from the magnetization component perpendicular to the surface; the other measures the Kerr effects from magnetization components parallel to the surface. I found that hysteresis loops of the in-plane magnetization components have unusual shapes unlike those typically found on YIG films epitaxially grown on gadolinium gallium garnet ($Gd_3Ga_5O_{12}$ or GGG) substrates. With the information on magnetization components along the other two directions, I can attribute the unusual shapes of these hysteresis loops to the often-neglected effect of magneto-static energy, which is enabled by movable domain walls in the YIG(100) sample.

II. EXPERIMENTAL PROCEDURES

A bulk YIG crystal has a nearly cubic magneto-crystalline anisotropy with easy axes along eight equivalent (111) directions. The cubic anisotropy energy density is given by $U_K = K_1\left(m_x^2 m_y^2 + m_y^2 m_z^2 + m_z^2 m_x^2\right) + K_2 m_x^2 m_y^2 m_z^2$, with the first and second anisotropy constants $K_1 = -6100$ erg/cm^3 and $K_2 = -260$ erg/cm^3 at room temperature.[16] m_x, m_y, and m_z are the directional cosines of the magnetization along cubic crystalline axes. In the absence of shape anisotropy, domain walls along (110) directions involve a significant energy penalty.

In this study, I use a YIG(100) disc, 0.46 mm in thickness and 5 mm in diameter, which was purchased from Deltronic Crystal Industries, Inc. (Dover, NJ). It is polished on both sides by the manufacturer, and no further treatment is done to the sample. The disc is mounted on a fused silica substrate with two strips of double-sticking tape near the edge. Using a homebuilt electromagnet, I can apply an in-plane magnetic field to the sample disc along the vertical direction or the horizontal direction up to 1800 Oe. All measurements are done with the sample in ambient.

Magneto-optic effects in a YIG crystal as a function of optical wavelength are known.[17,18] In the visible range, the crystal is opaque and has a Verdet constant that peaks to V = 1900°/cm (3.2 rad/mm) at 594 nm. In the near infrared range between 1300 and 2000 nm, the crystal becomes transparent. The Verdet constant is nearly real, and its magnitude is reduced to 700°/cm (1.2 rad/mm) at 780 nm and further down to 200°/cm (0.34 rad/mm) at 1330 nm. The low transmission loss at 1330 and 1.55 nm makes YIG crystals desirable material choices for devices, such as Faraday isolators. The Voigt parameter Q that appears in the optical dielectric tensor is related to the Verdet constant V (in rad/mm) by $Q = \frac{\lambda}{\pi\sqrt{\epsilon_{YIG}}} V$.[2] Here, λ is in unit of mm. The present work involves MO effects around $\lambda = 780$ nm. The imaginary part of the Voigt parameter $Q = Q' + iQ''$ is negligibly small, and the real part is $Q' = \frac{\lambda}{\pi\sqrt{\epsilon_{YIG}}} V = 1.4 \times 10^{-4}$ at $\lambda = 780$ nm with $\epsilon_{YIG} = 2.2$. This has important bearing on Sagnac interferometry systems when measuring different YIG magnetization components.[4–6]

Figure 1 shows a normal-incidence Sagnac interferometry microscope used in this study. It measures the Faraday effect from the out-of-plane component of the YIG sample magnetization. The working principle of a normal-incidence Sagnac interferometry microscope has been described in detail in an earlier report.[5] In the present study, the sample is mounted on two orthogonal linear stages so that it can be moved along x_m and y_m directions with a precision of 0.5 μm for image acquisition. After emerging from the polarization-maintaining (PM) fiber, a collimated 780 nm beam passes through a $\lambda/4$ wave-plate with its fast axis set to 45° from the slow axis of the fiber. The beam is then focused on the rear surface of the YIG(100) sample with a long working distance objective with a focal length $f_0 = 20$ mm. The FWHM diameter of the focused beam on the sample is 3 μm.

There are two modes of operation of this microscope. One is to have the beam focused on the front surface instead so that the
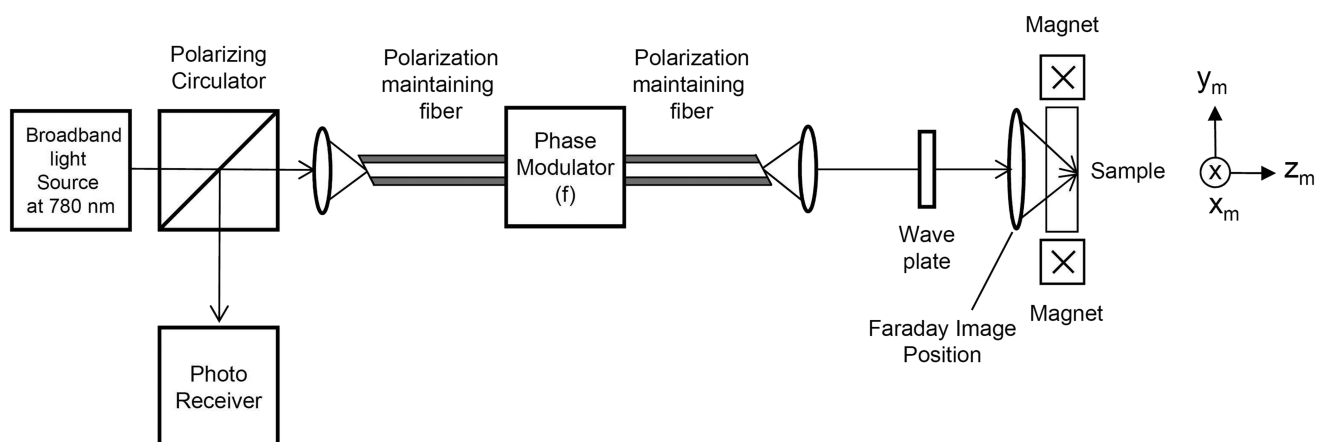

FIG. 1. Arrangement of the normal-incidence Sagnac interferometry scanning microscope in this study. The objective lens in front of the sample can be moved along the z_m direction so that the focus of the beam is at the rear surface for the Faraday rotation measurement. An electromagnet can be oriented to apply an in-plane field along either the x_m or y_m direction.

reflection is analyzed for the polar Kerr effect from the out-of-plane magnetization component. Kerr rotation is given by[5]

$$\theta_{K,P} \cong \mathrm{Re}\left\{-\frac{i\gamma_P Q m_z}{r_n}\right\}, \tag{1}$$

where r_n is the normal incidence reflectivity of the YIG crystal in air. γ_p is a function of optical dielectric constant ϵ_{YIG} of the YIG crystal at 780 nm. It is related to α_z in Ref. 5 by $\alpha_z = i\gamma_P Q$.[5,19] $m_z = m_{out-of-plane,\perp}$ is the directional cosine of the magnetization along the z_m direction. Since the YIG crystal is nearly transparent at 780 nm, both r_n and γ_p are real. As a result, the normal-incidence Sagnac interferometry microscope only measures the imaginary part Q'' of the Voigt parameter. As Q'' is negligibly small compared to the real part Q' at 780 nm, the Kerr effect given by Eq. (1) is not suitable for characterizing m_z. The other mode of operation as shown in Fig. 1 is to focus the beam on the rear surface of the sample disc so that the Sagnac interferometer measures the Faraday effect experienced by the beam as it traverses through the sample and back. The Faraday effect comes from Q'. As shown by the author in a recent work,[19] the Faraday rotation measured with the normal-incidence Sagnac interferometry microscope is given by

$$\theta_{F,P} = -\frac{\pi\sqrt{\epsilon_{YIG}}LQ'}{\lambda}m_z. \tag{2}$$

This rotation is large due to both Q' and a long interaction length L. The latter is twice the thickness of the sample. This makes it easy to image m_z and acquire hysteresis loops for this component.

Figure 2 shows an oblique-incidence Sagnac interferometry (OI-SA) system used in this study to measure Kerr effects arising from in-plane magnetization components (m_x and m_y). As shown in Ref. 5, by using a $\lambda/4$ wave-plate with its fast-axis (FA) at 45° from the p-polarization for wave-plate No. 1 placed before the sample and

a $\lambda/8$ wave-plate with its FA also at 45° from the p-polarization for wave-plate No. 2 after the sample, namely, a $\lambda/4$–$\lambda/8$ combination, the Sagnac interferometry system measures m_x as follows:[5]

$$\theta_{K,T} \cong \mathrm{Im}\left\{\frac{i2\gamma_T Q r_s m_x}{r_p^2 + r_s^2}\right\} \cong -\frac{2\gamma_T Q'}{r_s}m_x, \tag{3}$$

where m_x is the directional cosine of the sample magnetization in the x_m direction. γ_T is a function of the oblique incidence angle in air and ϵ_{YIG}. It is related to α_x in Refs. 5 and 19 by $\alpha_x = i\gamma_T Q$. For YIG(100), Eq. (3) is valid as the sample is nearly transparent at λ = 780 nm with ϵ_{YIG} = 4.84 and Q'' negligibly small. At θ_{inc} = 58°, the expected value of $|\theta_{K,T}| \cong \frac{2\sin\theta_{inc}Q'}{\epsilon_{YIG}-1}$ when m_x = 1 is 62 μrad, in good agreement with the measured value. Dividing $\theta_{K,T}$ by its maximum value $-2\gamma_T Q'/r_s$, I extract m_x.

By using a $\lambda/2$ wave-plate with its fast-axis (FA) at 22.5° from the p-polarization for wave-plate No. 1 placed before the sample and a $\lambda/4$ wave-plate with its FA parallel to the p-polarization for wave-plate No. 2 after the sample, namely, a $\lambda/2$–$\lambda/4$ combination, the Sagnac interferometry system measures m_y as follows:[5]

$$\theta_{K,L} \cong \mathrm{Im}\left\{\frac{i2\gamma_L Q(r_p - r_s)m_y}{r_p^2 + r_s^2}\right\} \cong -\frac{2\gamma_L Q'}{r_s}m_y, \tag{4}$$

where m_y is the directional cosine of the magnetization along the y_m direction. γ_L is related to α_y in Ref. 5 by $\alpha_y = i\gamma_L Q$. For YIG(100) at θ_{inc} = 58°, $\gamma_T \approx 2\gamma_L$. Dividing $\theta_{K,L}$ by its maximum value, $-2\gamma_L Q'/r_s$, I extract m_y.

The YIG(100) sample can be rotated about the surface normal so that the azimuth angle between the crystalline $\langle 100\rangle$ axis and the x_m direction is varied in the experiment. For in-plane magnetization measurements using the oblique-incidence Sagnac interferometry microscope (see Fig. 2), the sample disc is illuminated with a collimated beam with a diameter of 4 mm to yield the spatially averaged
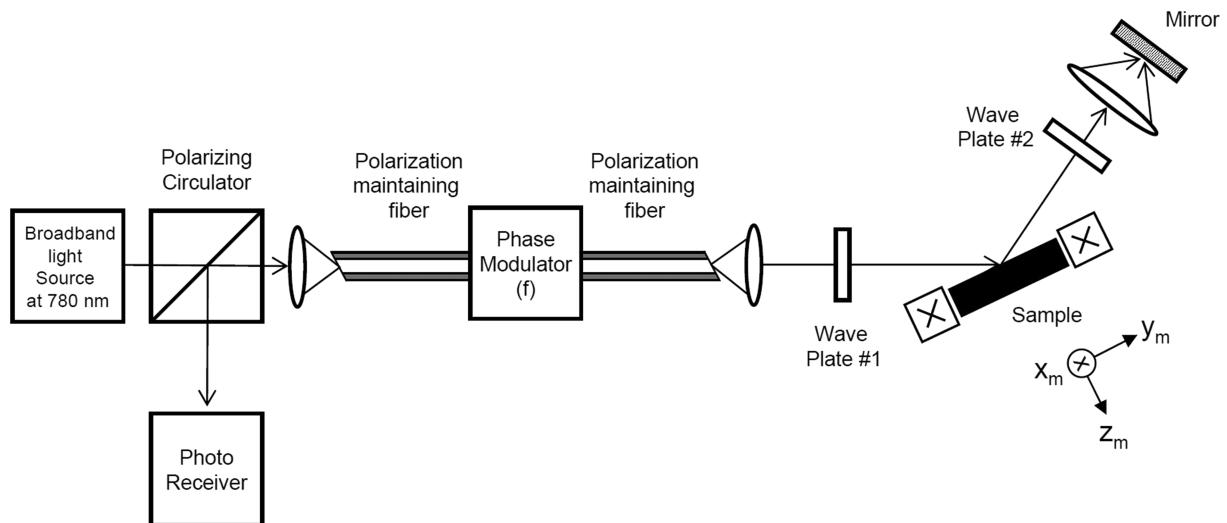

FIG. 2. Arrangement of the oblique-incidence Sagnac interferometry system used in this study. The optical beam that emerges from the polarization-maintaining fiber passes through wave-plate No. 1 before being incident on the sample at θ_{inc} = 58°. The reflected beam passes through wave-plate No. 2 and is then focused on a reflection mirror with a 10× objective. The mirror sends the beam along the same path back to the polarization-maintaining fiber. The electromagnet can be rotated to apply an in-plane field along the x_m direction or y_m direction.

in-plane magnetization, namely, $\langle m_x \rangle$ and $\langle m_y \rangle$. The average is in the x–y plane. For out-of-plane magnetization measurements using the normal-incidence Sagnac interferometry microscope, the sample is illuminated with a focused beam to yield a spatially resolved out-of-plane magnetization m_z (through Faraday rotation). Although m_z is spatially revolved in the x–y plane, it is averaged over the thickness of the sample along the z-axis.

III. UNUSUAL HYSTERESIS LOOPS OF IN-PLANE MAGNETIZATION IN AN IN-PLANE EXTERNAL FIELD

In the first set of experiments, I measure the hysteresis loops of $\langle m_{in\text{-}plane,\parallel} \rangle = \langle m_x \rangle$ by applying the external magnetic field along the x_m direction. The results are shown in Fig. 3. When the field is along the $\langle 100 \rangle$ axis [i.e., x_m parallel to the $\langle 100 \rangle$ axis; see Fig. 3(a)] and decreases from 150 Oe, $\langle m_{in\text{-}plane,\parallel} \rangle$ begins to decrease and gradually reaches nearly zero at around 60 Oe even before the field reverses the direction. $\langle m_{in\text{-}plane,\parallel} \rangle$ remains at zero as the field decreases to zero and further to −60 Oe. When the field decreases still further, $\langle m_{in\text{-}plane,\parallel} \rangle$ starts to decrease again and levels off beyond −150 Oe.

When the field is along the $\langle 110 \rangle$ direction [Fig. 3(b)] and decreases from 150 Oe, $\langle m_{in\text{-}plane,\parallel} \rangle$ again decreases gradually but not to zero when the field reaches 60 Oe. As the field decreases further from 60 to 50 Oe, it decreases steeply to 1/3–1/4 of its maximum value. It continues to decrease and reaches zero when the field is reduced to −50 Oe. When the field decreases further from −50 to −60 Oe, $\langle m_{in\text{-}plane,\parallel} \rangle$ decreases steeply from zero. Afterward, it slowly levels off as the field reaches −140 Oe. Obviously, the hysteresis loops shown in Fig. 3 seem rather unusual for ferromagnetic and ferrimagnetic samples. To understand how these atypical shapes come about requires further information on the magnetization components perpendicular to the external field.

In the second set of experiments, I measure the hysteresis loops of $\langle m_{in\text{-}plane,\perp} \rangle = \langle m_y \rangle$ with the external magnetic field again applied along the x_m direction. From $\langle m_{in\text{-}plane,\perp} \rangle$, I extract the averaged angle $\langle \phi \rangle$ between the in-plane magnetization and the external field.

In Fig. 4, I show $\langle \phi \rangle$ during the same hysteresis loop. With the field direction deviating from the $\langle 100 \rangle$ axis by small angles, $\langle \phi \rangle$ goes through a dramatic change as the field decreases from 200 to 90 Oe, while $\langle m_{in\text{-}plane,\parallel} \rangle$ changes but slightly [see Fig. 3(a)]. The in-plane magnetization clearly rotates away from the field direction toward the nearest of $\langle 110 \rangle$, $\langle 1\bar{1}0 \rangle$, $\langle \bar{1}10 \rangle$, and $\langle \bar{1}\bar{1}0 \rangle$ axes. For example, when the field is 15° clockwise from the $\langle 100 \rangle$ axis [see Fig. 4(a)], the averaged in-plane magnetization rotates toward the $\langle 1\bar{1}0 \rangle$ axis and $\langle \phi \rangle$ increases. As the field further decreases, $\langle \phi \rangle$ diminishes in magnitude slowly. It reaches zero when the field decreases to −60 Oe. When the field decreases further to −90 Oe, $\langle \phi \rangle$ decreases from zero steeply, indicating that the in-plane magnetization quickly rotates toward the $\langle \bar{1}10 \rangle$ axis. When the field decreases still further from −90 to −140 Oe, $\langle \phi \rangle$ now increases toward zero and the averaged in-plane magnetization rotates toward the external field. When the field is 15° counterclockwise from the $\langle 100 \rangle$ axis [see Fig. 4(c)], as the external field is reduced to 90 Oe, $\langle \phi \rangle$ decreases and the averaged in-plane magnetization rotates toward the $\langle 110 \rangle$ axis. In this case, $\langle \phi \rangle$ behaves the same as for the field being 15° clockwise from the $\langle 100 \rangle$ axis except for the negative sign. When the $\langle 100 \rangle$ axis is more or less parallel to the external field [see Fig. 4(b)], $\langle \phi \rangle \sim 0$, indicating that the averaged in-plane magnetization remains more or less parallel to the field.

In Fig. 5, I show $\langle \phi \rangle$ during the same hysteresis loop when the external field is near the $\langle 110 \rangle$ axis instead of the $\langle 100 \rangle$ axis. When the field deviates from the $\langle 110 \rangle$ axis by small angles, $\langle \phi \rangle$ again goes through a dramatic change from 200 to 90 Oe, indicating that the in-plane magnetization rotates toward the nearest of $\langle 110 \rangle$, $\langle 1\bar{1}0 \rangle$, $\langle \bar{1}10 \rangle$, and $\langle \bar{1}\bar{1}0 \rangle$ axes. When the field is 15° clockwise from the $\langle 110 \rangle$ axis [see Fig. 5(a)], the magnetization rotates toward the $\langle 110 \rangle$ axis at 90 Oe and $\langle \phi \rangle$ increases. As the field decreases from 90 to 60 Oe, $\langle \phi \rangle$ decreases but slowly and only becomes zero when the field reaches −60 Oe. As the field decreases further to −90 Oe, $\langle \phi \rangle$ decreases to below zero, indicating that the in-plane magnetization rotates toward the $\langle \bar{1}\bar{1}0 \rangle$ axis. As the field decreases still further to −140 Oe, $\langle \phi \rangle$ increases toward zero as the in-plane magnetization rotates toward the external field. When the field is 15° counterclockwise from the $\langle 110 \rangle$ axis [see Fig. 5(a)], the magnetization still rotates
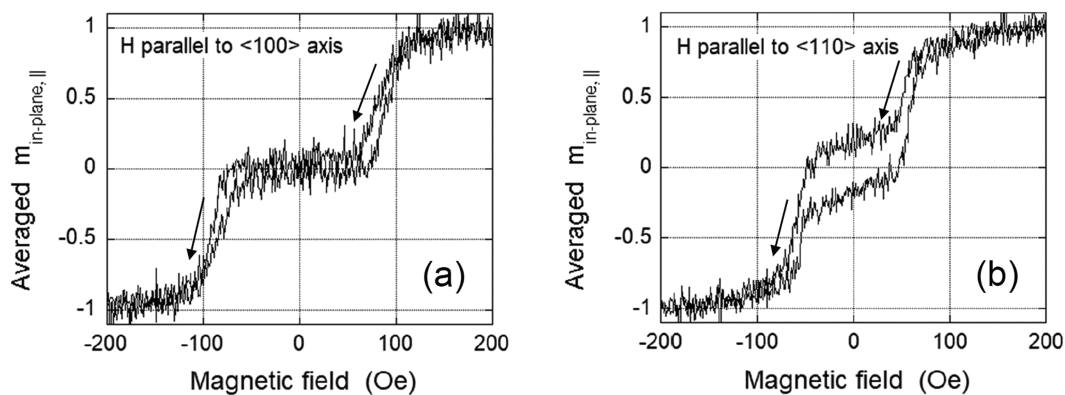

FIG. 3. Hysteresis loops of $\langle m_{in\text{-}plane,\parallel} \rangle$ with the external magnetic field applied along the x_m direction: (a) the x_m direction is parallel to the $\langle 100 \rangle$ axis and (b) the x_m direction is parallel to the $\langle 110 \rangle$ axis.
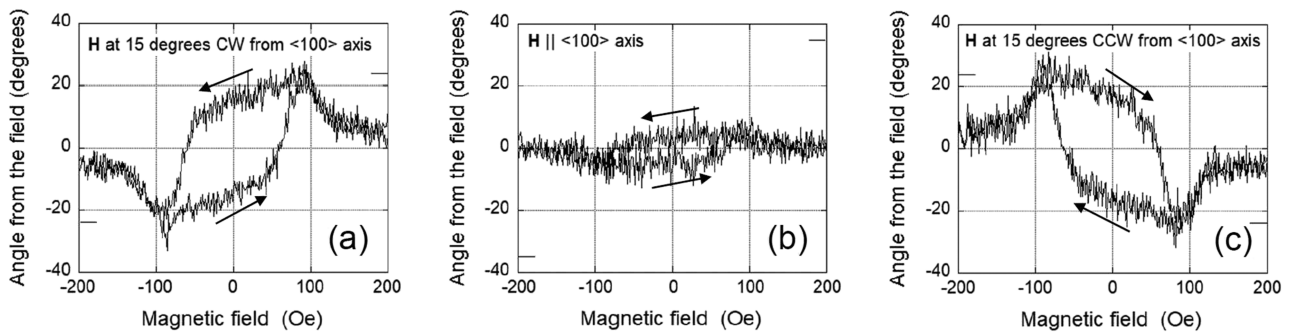
FIG. 4. Spatially averaged angles of the sample magnetization from the direction of the external field (i.e., the x_m direction) during the same hysteresis loop: (a) the field is 15° clockwise from the $\langle 100 \rangle$ axis; −24° marks the $\langle 1\overline{1}0 \rangle$ axis, while +24° marks the $\langle 110 \rangle$ axis; (b) the field is along the $\langle 100 \rangle$ axis; −35° marks the $\langle \overline{1}\overline{1}0 \rangle$ axis, while +35° indicates the $\langle 110 \rangle$ axis; and (c) the field is 15° counterclockwise from the $\langle 100 \rangle$ axis; +24° marks the $\langle 110 \rangle$ axis, while −24° indicates the $\langle \overline{1}\overline{1}0 \rangle$ axis.
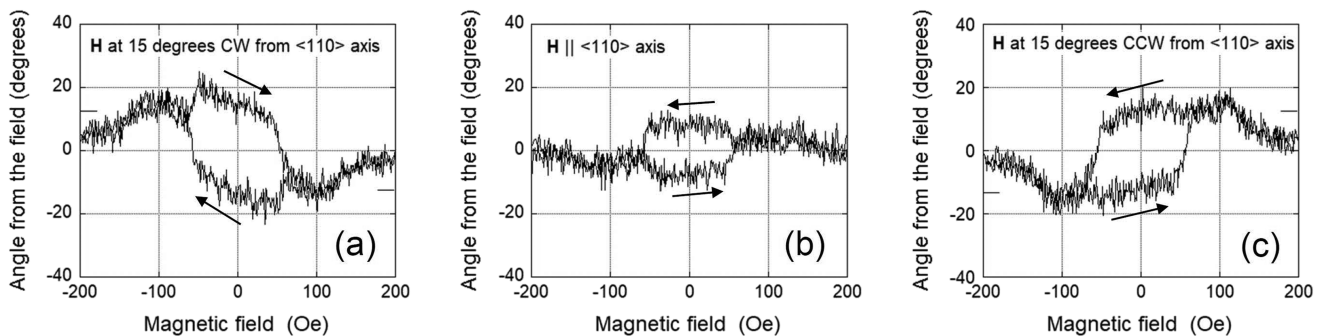

FIG. 5. Spatially averaged angles of the sample magnetization from the direction of the external magnetic field (i.e., the x_m direction) during the same hysteresis loop: (a) the field is 15° clockwise from the $\langle 110 \rangle$ axis; +12° marks the $\langle 110 \rangle$ axis, while −12° indicates the $\langle \overline{1}\overline{1}0 \rangle$ axis; (b) the field is along the $\langle 110 \rangle$ axis; and (c) the field is 15° counterclockwise rotated from the $\langle 110$ axis); −12° marks the $\langle 110 \rangle$ axis, while +12° indicates the $\langle \overline{1}\overline{1}0 \rangle$ axis.

toward the $\langle 110 \rangle$ axis at 90 Oe and $\langle \phi \rangle$ decreases in this case. In fact, $\langle \phi \rangle$ behaves similar to that when the field is 15° clockwise from the $\langle 110 \rangle$ axis except for the negative sign. Again, when the field direction is almost parallel to the $\langle 110 \rangle$ axis, $\langle \phi \rangle \sim 0$, indicating that the averaged in-plane magnetization is more or less parallel to the external field.

In the third set of experiments, I measured Faraday rotation $\theta_{F,P}$ during the same hysteresis loop with the field applied close to the $\langle 100 \rangle$ axis using the normal-incidence Sagnac interferometric microscope as shown in Fig. 1. By dividing $\theta_{F,P}$ with its maximum value, I deduce a normalized $m_{out\text{-}of\text{-}plane,\perp}$ value. Since the beam is focused on the rear surface of the sample to a diameter of 3 μm that is much smaller than magnetic domains in the sample (as will be clear shortly), the normalized $m_{out\text{-}of\text{-}plane,\perp}$ value is not spatially averaged and reveals local domain formation and domain wall movement. In Fig. 6(a), I show the normalized $m_{out\text{-}of\text{-}plane,\perp}$ value during five field ramp-ups. In Fig. 6(b), I show the normalized $m_{out\text{-}of\text{-}plane,\perp}$ value during five field ramp-downs for clarity. Above 140 Oe, the magnetization has no out-of-plane component and is thus aligned with the in-plane external field. As the field decreases from 140 to 80 Oe, an out-of-plane component emerges and quickly reaches the maximum values: $m_{out\text{-}of\text{-}plane,\perp} = -1$ for m_z pointing out of the sample

and $m_{out\text{-}of\text{-}plane,\perp} = +1$ for m_z pointing into the sample. This indicates the emergence (formation) of magnetic domains at 140 Oe and the dominance of crystalline anisotropy in the domain orientation at 80 Oe. As the field decreases to zero, $m_{out\text{-}of\text{-}plane,\perp}$ remains mostly at the maximum value, occasionally switching to the opposite maximum due to domain wall movement. When the field decreases below zero, $m_{out\text{-}of\text{-}plane,\perp}$ begins to switch more frequently between the two maxima until −80 Oe. When the field decreased further from −80 to −140 Oe, $m_{out\text{-}of\text{-}plane,\perp}$ quickly approaches zero from the maximum values, indicating that the magnetization is again aligned with the externally applied field.

IV. FARADAY EFFECT IMAGES OF MAGNETIC DOMAINS IN YIG(100) AT THE STAGES OF A HYSTERESIS LOOP

To examine domain structures further, I acquire a set of images of $m_{out\text{-}of\text{-}plane,\perp}$ at various stages of the hysteresis loop with the field applied along the $\langle 100 \rangle$ axis. The images are obtained with a step size (i.e., the pixel size) of 10 μm.
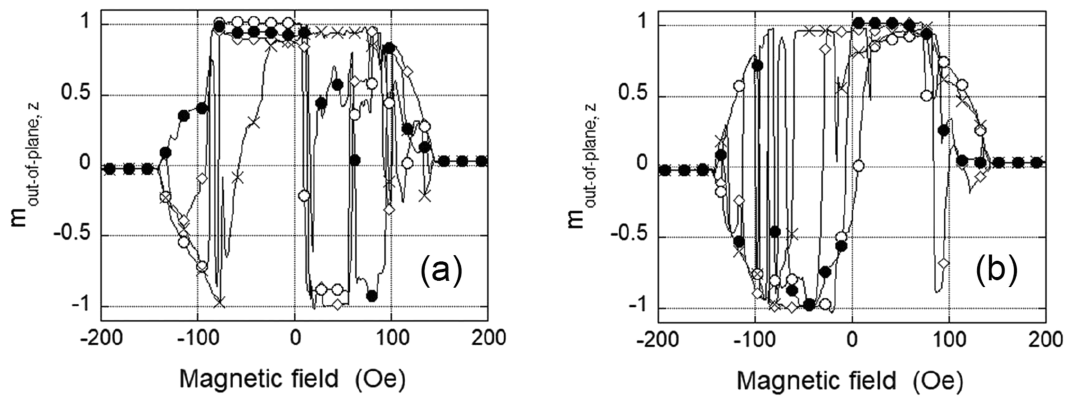
FIG. 6. Hysteresis loops of $m_{out-of-plane,\perp} = m_z$ from one spot on the sample when the external field is swept in the y_m direction: (a) m_z during the field ramp-up from -200 to $+200$ Oe and (b) m_z during the field ramp-down from $+200$ to -200 Oe.

In Fig. 7, I show obtained $m_{out-of-plane,\perp}$ images from an area of 600×600 μm^2 near the center of the sample as the field ramps up from -190 to $+190$ Oe. When the field is below -150 Oe, $m_{out-of-plane,\perp} \approx 0$ everywhere: the sample behaves as a single domain with the magnetization aligned parallel to the applied field. When the field increases above -140 Oe, a large number of magnetic domains emerge with the absolute magnitude of $m_{out-of-plane,\perp}$ significantly less than unity. Domains grow in size, while the absolute magnitude of $m_{out-of-plane,\perp}$ increases when the field increases to -80 Oe. $m_{out-of-plane,\perp}$ reaches its maximum values of ± 1 at -80 Oe, indicating that domains are aligned along easy axes. As the field increases further, the sizes and shapes of domains continue to evolve, while $m_{out-of-plane,\perp}$ remains more or less at ± 1, indicating that domain walls move about, while domains remain oriented along easy axes. Only when the field increases beyond 90 Oe, domains start to break down into smaller ones and the absolute magnitude of $m_{out-of-plane,\perp}$ starts to decrease, indicating that domains rotate away from easy axes and toward the external field. When the field is above 150 Oe, $m_{out-of-plane,\perp} = 0$ everywhere: domains disappear and the whole sample is aligned along the field.

I should note that Fig. 7 reveals magnetic domains but only in $m_{out-of-plane,\perp}$. As a result, "each domain" can contain sub-domains with different values of $m_{in-plane,\parallel}$ and $m_{in-plane,\perp}$. Starting at -85 Oe and becoming more obvious at -65 Oe during the field ramp-up, some regions with $m_{out-of-plane,\perp} > 0$ break into two sub-domains, while some other regions with $m_{out-of-plane,\perp} < 0$ also break into two sub-domains with noticeable contrasts.

V. DISCUSSION

With all three components of the YIG(100) sample magnetization measured during a hysteresis loop, what do we learn as to what happens in the sample as the field sweeps up and down? Can we understand unusual shapes of the hysteresis loops displayed in Fig. 3? What can one expect, in general, when a hysteresis loop is measured on a single crystal sample that contains a number of spatially uncharacterized domains?

From Fig. 4 through Fig. 7 together with Fig. 3, I can conclude that when the external field is above 140 Oe, the magnetization of the entire YIG(100) sample disc is aligned with the field with $\langle m_{in-plane,\parallel} \rangle = 1$. When the field decreases from 140 to 80 Oe, the sample breaks into domains that grow in size and slowly rotate toward the nearest easy axes with $m_{out-of-plane,\perp}$ and $\langle m_{in-plane,\perp} \rangle$ reaching their maximum values. This shows that the magnetization becomes dominated by the crystalline anisotropy. As the field decreases to zero and further to -60 Oe, domains redistribute to other easy axes by mostly domain wall movements, causing eventually $\langle m_{in-plane,\parallel} \rangle = 0$, $\langle m_{in-plane,\perp} \rangle = 0$, and $\langle m_{out-of-plane,\perp} \rangle = 0$. When the field continues to decrease from -60 to -80 Oe, domains redistribute to those along the easy axes that are nearest to the field direction by domain wall movements. As the field decreases from -80 to -140 Oe, domains break down into smaller ones and the magnetization gradually rotates toward the applied field. Details depend on the direction of the external field with respect to crystalline axes within the sample surface.

When the field is along the $\langle 100 \rangle$ axis, there are four nearest easy axes: $\langle 111 \rangle$, $\langle 11\bar{1} \rangle$, $\langle 1\bar{1}1 \rangle$, and $\langle 1\bar{1}\bar{1} \rangle$. When the field ramps down from 140 to 80 Oe, domains rotate from the field direction toward these easy axes. As a result, $\langle m_{in-plane,\parallel} \rangle$ decreases from 1 to $0.57 = \cos 54.7°$ as these easy axes are $54.7°$ from the field direction, while $\langle m_{in-plane,\perp} \rangle \cong 0$ as domains distribute among these easy axes equally, just as shown in Figs. 3(a) and 4(b). When the field decreases from 80 to 60 Oe, domains redistribute to remaining four easy axes evenly so that $\langle m_{in-plane,\parallel} \rangle \cong 0$ and $\langle m_{in-plane,\perp} \rangle \cong 0$. The equal distribution among all eight easy axes remains when the field decreases zero and further to -60 Oe. When the field decreases from -60 to -80 Oe, domains redistribute to those along four easy axes that are nearest to the field direction: $\langle \bar{1}11 \rangle$, $\langle \bar{1}1\bar{1} \rangle$, $\langle \bar{1}\bar{1}1 \rangle$, and $\langle \bar{1}\bar{1}\bar{1} \rangle$ axes. As a result, $\langle m_{in-plane,\parallel} \rangle$ decreases from 0 to $-0.57 = -\cos 54.7°$, while $\langle m_{in-plane,\perp} \rangle$ remains zero. When the field continues to decrease to -140 Oe, domains break down into smaller ones and rotate toward the field direction so that $\langle m_{in-plane,\parallel} \rangle$ approaches -1. The proposed description is summarized in Fig. 8.

When the field direction deviates from the $\langle 100 \rangle$ axis, for example, clockwise by $15°$, only $\langle 1\bar{1}1 \rangle$ and $\langle 1\bar{1}\bar{1} \rangle$ are the nearest easy
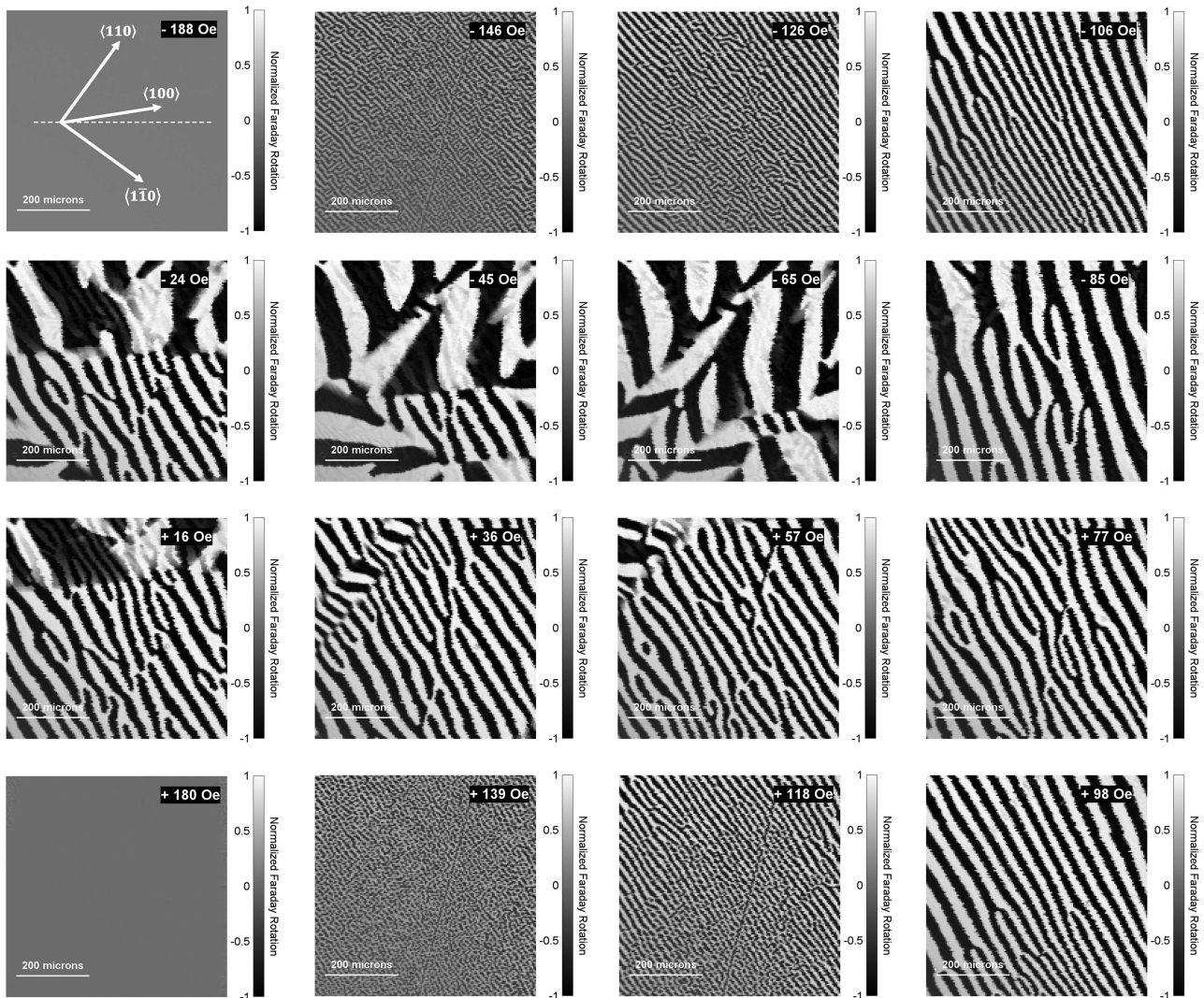
FIG. 7. Normalized $m_{out-of-plane,\perp}$ images of an area of $600 \times 600 \ \mu m^2$ on the YIG(100) sample at different stages of a hysteresis loop. The external field is applied along the y_m direction (dotted line) that is close to the $\langle 100 \rangle$ axis.
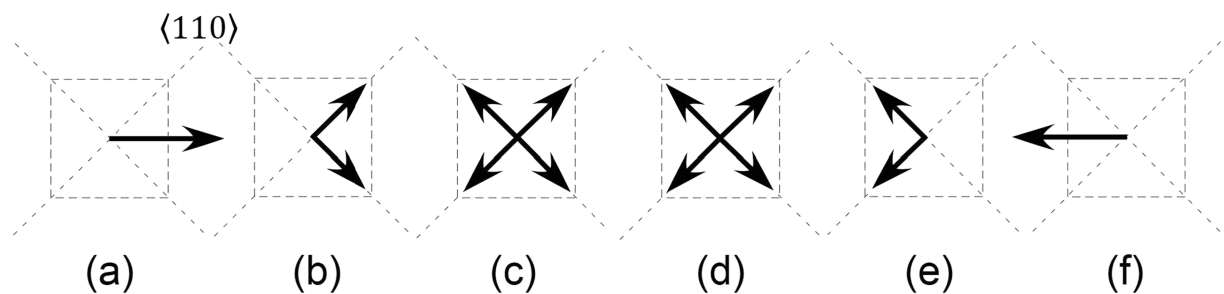

FIG. 8. Distribution of magnetic domain orientations in YIG(100) as a function of external field applied along the $\langle 100 \rangle$ axis: (a) H $\geq$ +150 Oe, (b) +80 Oe, (c) +60 Oe, (d) −60 Oe, (e) −80 Oe, and (f) H $\leq$ −160 Oe.

axes. As shown in Fig. 4(a), when the field ramps down from 140 to 80 Oe, domains rotate toward these two axes and $\langle \phi \rangle$ increases. At 80 Oe, $\langle \phi \rangle$ reaches 24.2°, which is the angle between the field direction and either of these two axes. As the field decreases from 80 to 60 Oe, domains redistribute to other easy axes somewhat so that $\langle \phi \rangle$ is reduced to 22°. When the field decreases to zero and further to −60 Oe, the redistribution of domains to all easy axes gradually becomes complete by both domain wall movement and domain rotation so that $\langle \phi \rangle$ approaches zero. When the field decreases further from −60 to −80 Oe, domains redistribute by a combination of domain wall movement and rotation to those along $\langle \bar{1}\bar{1}1 \rangle$ and $\langle \bar{1}\bar{1}\bar{1} \rangle$ and $\langle \phi \rangle$ reaches −24.2°. When the field decreases still further to −140 Oe, domains break down into smaller ones and gradually rotate toward the field direction, and thus, $\langle \phi \rangle$ diminishes. When the field direction deviates from the $\langle 100 \rangle$ axis counterclockwise by 15°, a similar scenario occurs except that as the field ramps down, $\langle 1\bar{1}1 \rangle$ and $\langle 1\bar{1}\bar{1} \rangle$ are the nearest easy axes initially, and thus, $\langle \phi \rangle$ behaves as shown in Fig. 4(c). This description is illustrated in Fig. 9.

When the field direction is along the $\langle 110 \rangle$ axis, $\langle 111 \rangle$ and $\langle 11\bar{1} \rangle$ are the two nearest easy axes. When the field ramps down from 140 to 80 Oe, domains form and rotate toward these two axes with equal propensity. As a result, $\langle m_{in\text{-}plane,\parallel} \rangle$ decreases from 1 to 0.82 = cos 35.3° as these axes are 35.3° from the field direction and $\langle \phi \rangle \approx 0$, just as shown in Figs. 3(b) and 5(b). When the field decreases from 80 to 60 Oe, domains begin to redistribute but only among six easy axes, $-\langle 111 \rangle$, $11\bar{1}$ $1\bar{1}1$, $\langle 1\bar{1}\bar{1} \rangle$, $\langle \bar{1}11 \rangle$, and $\langle \bar{1}1\bar{1} \rangle$, nearly equally so that $\langle m_{in\text{-}plane,\parallel} \rangle$ is reduced by a factor of 3 from 0.82 to 0.27 and $\langle \phi \rangle$ remains zero. Domains redistribute to all eight easy axes gradually

by a combination of domain wall movement and domain rotation when the field decreases to zero and further to −60 Oe, leading to $\langle m_{in\text{-}plane,\parallel} \rangle = 0$ and $\langle \phi \rangle = 0$. When the field (now along the $\langle \bar{1}\bar{1}0 \rangle$ axis) decreases from −60 to −80 Oe, domains redistribute again by wall movement and rotation to those along $\langle \bar{1}\bar{1}1 \rangle$ and $\langle \bar{1}\bar{1}\bar{1} \rangle$, which are the nearest to the field direction. As a result, $\langle m_{in\text{-}plane,\parallel} \rangle$ decreases from 0 to −0.82 = −cos 35.3°, while $\langle \phi \rangle$ remains zero. As the field continues to decrease to −140 Oe, domains break down and gradually rotate toward the field direction, and thus, $\langle m_{in\text{-}plane,\parallel} \rangle$ reaches −1. The summary is illustrated in Fig. 10.

When the field direction deviates from the $\langle 110 \rangle$ axis, for example, counterclockwise by 15°, $\langle 111 \rangle$ and $\langle 11\bar{1} \rangle$ are the nearest easy axes. When the field ramps down from 140 to 80 Oe, domains form and rotate toward these axes so that $\langle \phi \rangle$ increases and reaches 0.21 = sin 12.3° as these axes are 12.3° from the field direction, just as shown in Fig. 5(c). As the field decreases from 80 to 60 Oe, domains begin to redistribute to other easy axes and $\langle \phi \rangle$ is reduced. When the field decreases further to zero and eventually to −60 Oe, the redistribution of domains becomes complete by a combination of domain wall movement and domain rotation, and thus, $\langle \phi \rangle$ reaches zero. When the field decreases further from −60 to −80 Oe, domains rotate to only those along $\langle \bar{1}\bar{1}1 \rangle$ and $\langle \bar{1}\bar{1}\bar{1} \rangle$ so that $\langle \phi \rangle$ decreases, −0.21 = −sin 12.3°. When the field decreases again from −80 to −140 Oe, domains break down and rotate toward the field direction, and in turn, $\langle \phi \rangle$ diminishes. If the field direction initially deviates from the $\langle 110 \rangle$ axis by 15° clockwise, $\langle 111 \rangle$ and $\langle 11\bar{1} \rangle$ are still the nearest easy axes initially; a similar scenario occurs during a field ramp down except that the sign of $\langle \phi \rangle$ is reversed [see Fig. 5(a)]. This description is summarized in Fig. 11.
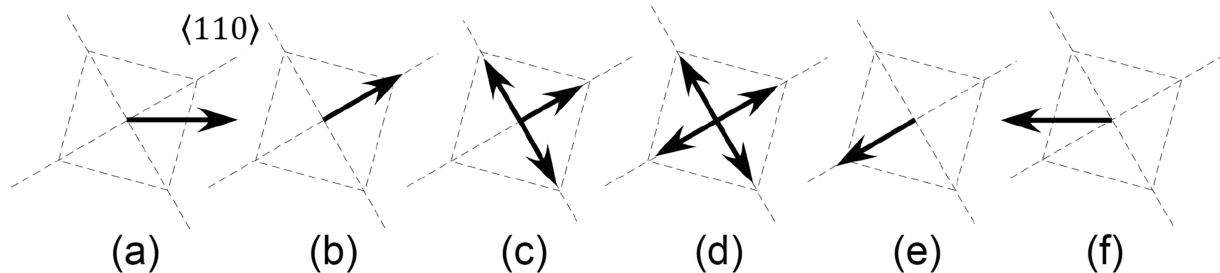

FIG. 9. Distribution of magnetic domain orientations in YIG(100) as a function of external field applied in the direction 15° clockwise from the $\langle 100 \rangle$ axis: (a) H ≥ 150 Oe, (b) +80 Oe, (c) +60 Oe, (d) −60 Oe, (e) −80 Oe, and (f) H ≤ −160 Oe.
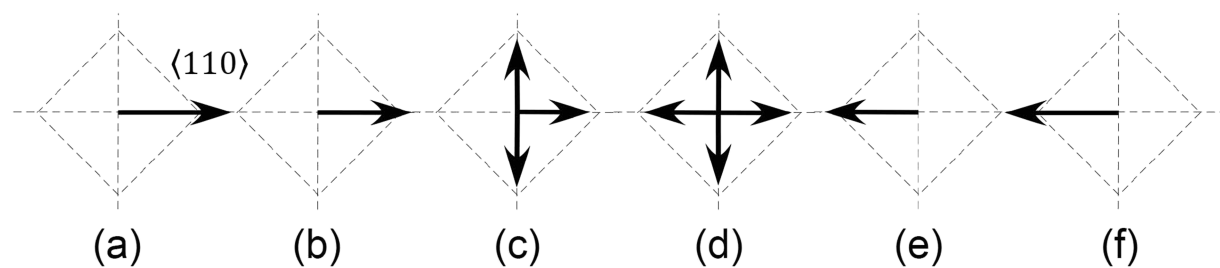

FIG. 10. Distribution of magnetic domain orientations in YIG(100) as a function of external field applied along the $\langle 110 \rangle$ axis: (a) H ≥ 150 Oe, (b) +80 Oe, (c) +60 Oe, (d) −60 Oe, (e) −80 Oe, and (f) H ≤ −160 Oe.
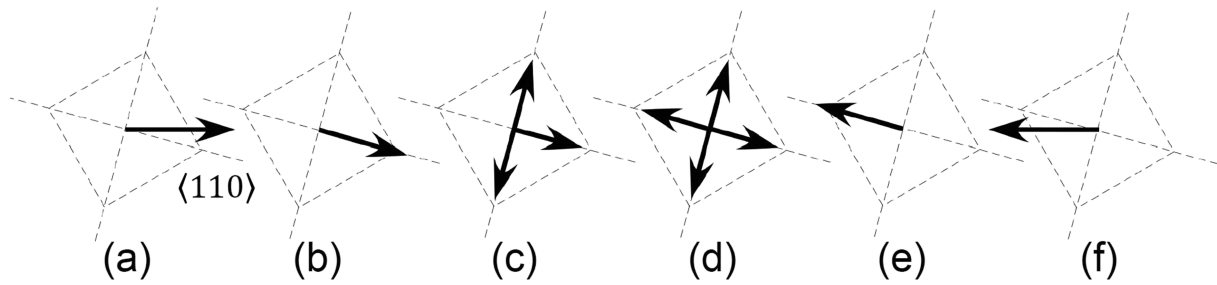
FIG. 11. Distribution of magnetic domain orientations in YIG(100) as a function of external field applied in the direction 15° clockwise from the $\langle 110 \rangle$ axis: (a) H ≥ 150 Oe, (b) +80 Oe, (c) +60 Oe, (d) −60 Oe, (e) −80 Oe, and (f) H ≤ −160 Oe.

The summarized behaviors of domains and hysteresis loops for a bulk YIG(100) crystal are unlike those of YIG crystalline films epitaxially grown on gadolinium gallium garnet (GGG) substrates,[20–24] YIG nanostructures,[25–28] and most ferromagnetic/ferrimagnetic crystals in forms of thin films or otherwise.[29–32] Typically, domain wall movements are limited and only play a minor role in the "early" part of a hysteresis loop.[33–39] This is not the case for the present YIG(100) crystal sample. It is obvious that here domain wall movements play a dominating role during the entire hysteresis loop and has facilitated domain redistribution from some easy axes to other easy axes before the field is reversed, presumably driven by the magneto-static energy.

Analyses of hysteresis loops measured on ferromagnetic and ferrielectric materials are mostly based on the original work of Stoner and Wohlfarth.[33–39] In fact, the Stoner–Wohlfarth model or its variations explain most observed hysteresis loops qualitatively and, in some cases, even quantitatively. The central elements of the model are (1) single domains without movable domain walls, (2) anisotropy energies arising from the intrinsic crystalline anisotropy and shapes of the magnetic domain, and (3) the Zeeman energy in the presence of an external magnetic field. By not allowing for formation of movable domain walls, the magneto-static energy that drives anti-parallel domain alignments plays essentially no role and is thus excluded in the analysis of hysteresis loops. The assumption of having no movable domain walls is justified when the sizes of domains are small, and thus, the formation of such walls is energetically unfavorable. However, for sufficiently large and homogeneous single crystal samples, the sizes of domains can be large enough to sustain one or more movable domain walls. In these cases, the Stoner–Wohlfarth model needs to be modified to include the magneto-static energy and in turn predicts new behaviors as observed in the present work. The propensity to minimizing the magneto-static energy causes domains separated by movable walls to change their relative proportions such that one domain can grow at the expense of its neighbor and vice versa.

I consider a modified Stoner–Wohlfarth model with the following key assumption: (1) the magneto-static energy as the driving force for domain redistribution; (2) one domain wall is allowed to form and move about; (3) domain rotation becomes important only when the field reversal is sufficiently large; and (4) an external magnetic field $\boldsymbol{H}$ is applied parallel or anti-parallel to the easy axis. Let θ be the angle between the magnetization of a single domain and the easy axis and H the magnitude of the field $\boldsymbol{H}$: H > 0 when the field

is parallel to the easy axis and H < 0 when the field is anti-parallel to the easy axis. The energy per unit volume is given by

$$E(\theta, f) = K_u \sin^2 \theta - (2f - 1)HM_s \cos \theta - Ag(f). \quad (5)$$

The first term is the crystalline anisotropy with $K_u > 0$. It comes from the first term of the cubic anisotropy energy, $K_1 \left(m_x^2 m_y^2 + m_y^2 m_z^2 + m_z^2 m_x^2 \right) + K_2 m_x^2 m_y^2 m_z^2$. I neglect the much smaller contribution from the K_2 term to simplify the discussion. The second term in Eq. (5) is the Zeeman energy due to the external field H. M_s is the saturation magnetization in a single domain and is temperature dependent as usual. f is the fraction of domains that orient at an angle θ from the easy axis, and $(1 - f)$ is the fraction of domains that orient at angle $\pi - \theta$ from the easy axis. The third term is the magneto-static energy with A > 0. $g(f)$ is a function that narrowly peaks to unity at $f = 1/2$. This term leads to the formation of "anti-parallel" domains separated by movable domain walls. The equilibrium values of θ_0 and f_0 minimize $E(\theta, f)$ and yield an averaged magnetization along the field direction as

$$\langle M \rangle = (2f_0 - 1)M_s \cos \theta_0. \quad (6)$$

In the absence of the magneto-static energy ($A = 0$), $\theta_0 = 0$, $f_0 = 1$, and $\langle M \rangle = M_s$ for $H > -2K_u/M_s$. For $H < -2K_u/M_s$, $\theta_0 = \pi$, $f_0 = 1$, and $\langle M \rangle = -M_s$. This prescribes a typical hysteresis loop when the field is applied along an easy axis.

In the absence of the external field (ie., $H = 0$), $\theta_0 = 0$, $f_0 = 1/2$, and $\langle M \rangle = 0$ as the sample consists of equal portions of domains having anti-parallel alignments. This is expected for a bulk crystalline ferromagnet material in zero field if domain walls exist and are allowed to move about.

When both an external field and the magneto-static energy are present, $\theta_0 = 0$ when $H > -2K_u/(2f - 1)M_s$. $f_0 = 1$ only when $H > A/M_s$ and $\langle M \rangle = M_s$. When $A/M_s > H > -2K_u/M_s$, $f_0 = 1/2$ and $\langle M \rangle = 0$. This prescription fits what is shown in Fig. 3(a) and requires the existence of a freely movable domain wall. Clearly, if domain sizes are restricted by the physical dimension of a sample or imperfections in the sample such that the formation of a movable domain wall is too costly, this prescription fails as the influence of the magneto-static energy is suppressed. YIG thin films,[20–24] YIG nanostructures,[25–28] and many bulk ferromagnetic/ferrimagnetic crystals are examples.[29–32]

For the YIG(100) sample investigated in the present work, the experimental evidence suggests that in a homogeneous part of the

sample, one movable domain wall is energetically permitted. Consider the hysteresis loop [Fig. 3(a)] obtained when the field along the $\langle 100 \rangle$ axis ramps down from 80 to 0 Oe. At 80 Oe, domains equally distribute among four easy axes: $\langle 111 \rangle$, $\langle 11\bar{1} \rangle$, $\langle 1\bar{1}1 \rangle$, and $\langle 1\bar{1}\bar{1} \rangle$. I apply the model to domains along one of them. Below 80 Oe, domains initially along the $\langle 111 \rangle$ axis become a mixture of those along $\langle 111 \rangle$ (with a fraction f) and those along $\langle \bar{1}11 \rangle$ (with a fraction $1 - f$). Two such domains are separated by one domain wall along the $\langle 011 \rangle$ direction. Since the $\langle 111 \rangle$ axis is $54.7°$ from the field direction, the total energy density is as follows:

$$E(\theta, f) = K_u \sin^2\theta - (2f - 1)H \cos 54.7° M_s \cos\theta - Ag(f). \quad (7)$$

When $H \cong 80$ Oe and $H \cos 54.7° > A/M_s$, I have $\theta_0 = 0$, $f_0 = 1$, and $\langle M \rangle = \cos 54.7° M_s = 0.57 M_s$. When $H \le 60$ Oe and $H \cos 54.7° < A/M_s$, I have instead $\theta_0 = 0$, $f_0 \approx 1/2$, and $\langle M \rangle \approx 0$. This analysis applies to domains along $\langle 11\bar{1} \rangle$ (paired with $\langle \bar{1}1\bar{1} \rangle$), $\langle 1\bar{1}1 \rangle$ (paired with $\langle \bar{1}\bar{1}1 \rangle$), and $\langle 1\bar{1}\bar{1} \rangle$ (paired with $\langle \bar{1}\bar{1}\bar{1} \rangle$). As a result, this model explains the hysteresis loop in Fig. 3(a). In a field ramp-up (see Fig. 7), the formation of sub-domains is noticeable at −85 Oe and becomes more obvious at −65 Oe. The contrasts from sub-domains have the opposite $m_{in\text{-}plane,\parallel}$ value but the same $m_{in\text{-}plane,\perp}$ and $m_{out\text{-}of\text{-}plane,\perp}$ values that presumably come from the nonlinear magneto-optic effect (i.e., the Voigt effect).

Now, consider the hysteresis loop when the field direction is along the $\langle 110 \rangle$ axis. At 80 Oe, domains are aligned along $\langle 111 \rangle$ and $\langle 11\bar{1} \rangle$ axes. Below 80 Oe, they begin to redistribute so that a fraction f of them remains along $\langle 111 \rangle$ and $\langle 11\bar{1} \rangle$ axes. The remaining domains are along $\langle \bar{1}11 \rangle$, $\langle 1\bar{1}1 \rangle$, $\langle 1\bar{1}\bar{1} \rangle$, and $\langle \bar{1}1\bar{1} \rangle$ axes. They are separated from those along $\langle 111 \rangle$ and $\langle 11\bar{1} \rangle$ axes by one domain wall. As a result, few or no domains are along $\langle \bar{1}\bar{1}1 \rangle$ and $\langle \bar{1}\bar{1}\bar{1} \rangle$ as they are two domain walls from domains along $\langle 111 \rangle$ and $\langle 11\bar{1} \rangle$ axes. Since $\langle 111 \rangle$ and $\langle 11\bar{1} \rangle$ axes are $35.3°$ from the field direction, while $\langle \bar{1}11 \rangle$, $\langle 1\bar{1}1 \rangle$, $\langle 1\bar{1}\bar{1} \rangle$, and $\langle \bar{1}1\bar{1} \rangle$ axes are perpendicular to the field, the total energy density is given by

$$E(\theta, f) = K_u \sin^2\theta - fH \cos 35.3° M_s \cos\theta - Ag(f), \quad (8)$$

$$\langle M \rangle = f M_s \cos 35.7°. \quad (9)$$

$g(f)$ peaks to unity at $f = 1/3$. When $H \cong 80$ Oe and $H \cos 35.3° > A/M_s$, I arrive at $\theta_0 = 0$, $f_0 = 1$, and $\langle M \rangle = \cos 35.3° M_s = 0.82 M_s$. When $H \le 50$ Oe and $H \cos 35.3° < A/M_s$, I have instead $\theta_0 = 0$, $f_0 \approx 1/3$, and $\langle M \rangle \approx 0.27 M_s$. As a result, this model also explains the experimental observation shown in Fig. 3(b). At 50 Oe, I indeed observed $\langle m_{in\text{-}plane,\parallel} \rangle \cong 0.27$. As the field continues to decrease, domains along $\langle \bar{1}\bar{1}1 \rangle$ and $\langle \bar{1}\bar{1}\bar{1} \rangle$ axes start to appear by domain rotation. At around −60 Oe, domains are evenly distributed among all easy axes and $\langle m_{in\text{-}plane,\parallel} \rangle \cong 0$.

VI. CONCLUSION

Domain redistributions, first to the easy axes nearest to the field direction and then to other easy axes before the field reversal, can take place in ferromagnetic or ferrimagnetic crystals and yield unusual hysteresis loops just like what are shown in Fig. 3. Attempts to interpret unusual hysteresis loops can be problematic if measurements are only done on the whole sample and for the

magnetization component in the field direction. By measuring all three components of the magnetization vector in a YIG(100) crystal through Kerr effects and the Faraday effect, I found that freely movable domain walls play a prominent role in determining orientations of magnetic domains and in turn the unusual appearances of hysteresis loops as illustrated in Fig. 3. It is reasonable to expect that sufficiently large and homogeneous ferromagnetic or ferrimagnetic crystals should behave similarly as they are capable of supporting movable domain walls and in turn enabling the magneto-static energy to play an often-neglected role in the domain orientation and distribution. Interestingly, hysteresis loops from polycrystalline and many crystalline samples usually have textbook-like appearances such that the magnetization of the whole sample does not vanish or behaves step-like as in Fig. 3 when the external field reaches zero from either direction. Presumably either movable domain walls in these samples are absent or wall movements are restricted by inhomogeneity.

ACKNOWLEDGMENTS

DATA AVAILABILITY

The data that support the findings of this study are available from the corresponding author upon reasonable request.

REFERENCES

[1] J. McCord, J. Phys. D: Appl. Phys. **48**, 333001 (2015).
[2] R. P. Hunt, J. Appl. Phys. **38**, 1652 (1967).
[3] Z. Q. Qiu and S. D. Bader, Rev. Sci. Instrum. **71**, 1243 (2000).
[4] A. Fried, M. Fejer, and A. Kapitulnik, Rev. Sci. Instrum. **85**, 103707 (2014).
[5] X. D. Zhu, Rev. Sci. Instrum. **88**, 083112 (2017).
[6] X. D. Zhu, R. Ullah, and V. Taufour, Rev. Sci. Instrum. **92**, 043706 (2021).
[7] U. Hartmann, Annu. Rev. Mater. Sci. **29**, 53 (1999).
[8] X. Zhu, P. Grutter, V. Metlushko, and B. Ilic, Phys. Rev. B **66**, 024423 (2002).
[9] L. Yue and S. H. Liou, in *Scanning Probe Microscopy in Nanoscience and Nanotechnology*, edited by B. Bhushan (Springer, Berlin, Heidelberg, 2011), Vol. 2.
[10] O. Kazakova, R. Puttock, C. Barton, H. Corte-León, M. Jaafar, V. Neu, and A. Asenjo, J. Appl. Phys. **125**, 060901 (2019).
[11] J. Stöhr, H. A. Padmore, S. Anders, T. Stammler, and M. R. Scheinfein, Surf. Rev. Lett. **5**, 1297 (1998).
[12] T. Funk, A. Deb, S. J. George, H. Wang, and S. P. Cramer, Coord. Chem. Rev. **249**, 3 (2005).
[13] A. Mascaraque, L. Aballe, J. F. Marco, T. O. Menteş, F. El Gabaly, C. Klein, A. K. Schmid, K. F. McCarty, A. Locatelli, and J. de la Figuera, Phys. Rev. B **80**, 172401 (2009).
[14] S. Ruoß, C. Stahl, M. Weigand, G. Schütz, and J. Albrecht, Appl. Phys. Lett. **106**, 022601 (2015).
[15] A. S. Tang, J. Pelliciari, Q. Song, Q. Song, S. Ning, J. W. Freeland, R. Comin, and C. A. Ross, Phys. Rev. Mater. **3**, 054408 (2019).
[16] M. Wu, J. Phys. C: Solid State Phys. **62**, 163 (2021).
[17] C. D. Mee, Contemp. Phys. **8**, 385 (1967).
[18] T. Boudiar, B. Payet-Gervy, M.-F. Blanc-Mignon, J.-J. Rousseau, M. Le Berre, and H. Joisten, J. Magn. Magn. Mater. **284**, 77 (2004).
[19] X. D. Zhu, OSA Continuum **4**, 966 (2021).

[20] A. A. Jalali, S. Kahl, V. Denysenkov, and A. M. Grishin, Phys. Rev. B **66**, 104419 (2002).

[21] C. Hauser, T. Richter, N. Homonnay, C. Eisenschmidt, M. Qaid, H. Deniz, D. Hesse, M. Sawicki, S. G. Ebbinghaus, and G. Schmidt, Sci. Rep. **6**, 20827 (2016).

[22] G. Li, H. Bai, J. Su, Z. Z. Zhu, Y. Zhang, and J. W. Cai, APL Mater. **7**, 041104 (2019).

[23] C. Tang, M. Aldosary, Z. Jiang, H. Chang, B. Madon, K. Chan, M. Wu, J. E. Garay, and J. Shi, Appl. Phys. Lett. **108**, 102403 (2016).

[24] H. Chang, T. Liu, D. Reifsnyder Hickey, P. A. P. Janantha, K. A. Mkhoyan, and M. Wu, APL Mater. **5**, 126104 (2017).

[25] H. Zheng, M. Han, L. Zheng, P. Zheng, Q. Wu, L. Deng, and H. Qin, Appl. Phys. Lett. **107**, 062401 (2015).

[26] M. N. Akhtar, A. Bakar Sulong, M. A. Khan, M. Ahmad, G. Murtaza, M. R. Raza, R. Raza, M. Saleem, and M. Kashif, J. Magn. Magn. Mater. **401**, 425 (2016).

[27] S. Hosseinzadeh, M. Behboudnia, L. Jamilpanah, M. H. Sheikhi, E. Mohajerani, K. Tian, A. Tiwari, P. Elahi, and S. M. Mohseni, J. Magn. Magn. Mater. **476**, 355 (2019).

[28] G. Venkat, T. A. Rose, C. D. W. Cox, G. B. G. Stenning, A. J. Caruana, and K. Morrison, Europhys. Lett. **126**, 37001 (2019).

[29] T. T. Smith, Phys. Rev. **15**, 345 (1920).

[30] O. Heczko, J. Drahokoupil, and L. Straka, J. Appl. Phys. **117**, 17E703 (2015).

[31] O. Ozdemir, Geophys. J. Int. **141**, 351 (2000).

[32] S. Takahashi, S. Kobayashi, and T. Shishido, J. Magn. Magn. Mater. **322**, 3658 (2010).

[33] E. C. Stoner and E. P. Wohlfarth, Philos. Trans. R. Soc. London, Ser. A **240**, 599 (1948).

[34] E. C. Stoner and E. P. Wohlfarth, IEEE Trans. Magn. **27**, 3475 (1991).

[35] D. L. Atherton and J. R. Beattie, IEEE Trans. Magn. **26**, 3059 (1990).

[36] C. Tannous and J. Gieraltowski, Eur. J. Phys. **29**, 475 (2008).

[37] S. A. Mathews, A. C. Ehrlich, and N. A. Charipar, Sci. Rep. **10**, 15141 (2020).

[38] R. V. Lapshin, Rev. Sci. Instrum. **91**, 065106 (2020).

[39] I. F. Lyuksyutov, T. Nattermann, and V. Pokrovsky, Phys. Rev. B **59**, 4260 (1999).